Journal of Materials Chemistry A

ROYAL SOCIETY OF CHEMISTRY

PAPER

View Article Online
View Journal | View Issue

Open Access Article. Published on 06 spalio 2025. Downloaded on 2026-02-13 14:41:43.
This article is licensed under a Creative Commons Attribution-NonCommercial 3.0 Unported Licence.

Check for updates

Cite this: J. Mater. Chem. A, 2025, 13, 36375

Decoding chemical structure–interface correlation in covalent organic framework for sustainable organic electrosynthesis

Rundong Wang, Ipsita Nath,* Jeet Chakraborty, Linyang Wang and Pascal Van Der Voort *

Received 9th July 2025
Accepted 27th September 2025

DOI: 10.1039/d5ta05552k

rsc.li/materials-a

Covalent Organic Frameworks (COFs) are a promising class of next-generation sustainable catalysts. Their robust backbones and tunable chemical structures offer them unique physicochemical properties. Conjugated COFs also show semiconducting behavior, which makes them suitable for charge and mass transfer processes. These features position COFs as strong candidates for electrocatalysis. However, their electrocatalytic performance is not yet well understood. In particular, there is limited knowledge about their interfacial structure and properties, which hinders their broader application. We herein report conjugated, highly porous COF-electrodes to address these issues, using the oxidation of benzylamine derivatives coupled with parallel cathodic hydrogen production as a model electrocatalytic system. We investigated the structure of the catalyst–medium interface and studied its potential-dependent capacitive and impedance behavior. By tuning the COF's physicochemical structure, we identified *operando* hydrogen bonding and surface adsorption interactions between the substrates and electrodes, which impacted the overall electrocatalytic performance. This first-of-its-kind, proof-of-concept study establishes the effectiveness of COFs as sustainable electrocatalysts and highlights the role of their physicochemical tuning in controlling the catalytic activities.

1 Introduction

Catalyzing chemical transformations in a green and sustainable way is central to addressing the combined challenges of energy, environmental protection, and sustainability, the so-called energy–environment–sustainability nexus. It is essential for achieving carbon neutrality and net zero. Electrocatalysis plays a key role in sustainable chemical synthesis.[1] It offers an efficient way to transfer electrons to or from molecules, enabling the making or breaking of chemical bonds. It also allows access to reaction pathways and intermediates that are otherwise difficult to achieve, thereby expanding the space for advanced chemical transformations.[2–4] As a result, organic electrosynthesis has recently gained significant attention.[5–7]

Despite this progress, the fundamental physical mechanisms behind these processes remain underexplored. In particular, the impedance and (pseudo)capacitive behavior of electrodes and the electrode–medium interface—which strongly influence the thermodynamics and kinetics of electrochemical reactions—are not well understood.[8–10] Gaining insight into these aspects could accelerate innovation in electrosynthesis and support the integration of these systems into industrial and societal applications. Combining organic electrosynthesis with hydrogen production can further improve the sustainability and cost-effectiveness of the process.

Recently, a variety of porous materials have been used in electro-organic synthesis due to their ability to support interfacial engineering.[11,12] Since charge and mass transfer occur at the electrode–medium interface, these materials have shown promising catalytic activity.[13] Among them, two-dimensional covalent organic frameworks (2D COFs) offer several advantages as next-generation porous electrodes, particularly in enabling precise tuning of interfacial interactions. These crystalline frameworks offer robust backbones, high surface area, ordered nanoporosity, extended conjugation, and semiconducting properties.[14–16] Given that electrochemistry is inherently a surface phenomenon, the high surface area and ordered porous channels of COFs can significantly enhance charge and mass transport during catalysis.[17–19] On the other hand, the semiconducting nature of the materials could ensure their charge accumulation and transport properties, enabling better control over the interface and electrical double layer (EDL).[20,21]

To date, most studies on COFs in electrochemistry have focused on energy storage and selected electrocatalytic reactions such as CO_2 reduction,[22] hydrogen evolution,[23] oxygen reduction,[24] and water oxidation.[25] However, the extensive use of COFs as electrodes for wider electrocatalytic processes,

COMOC—Center for Ordered Materials, Organometallics and Catalysis, Department of Chemistry, Ghent University, Krijgslaan 281, Building S3, 9000 Ghent, Belgium. E-mail: inath.nath@ugent.be; pascal.vandervoort@ugent.be

Open Access Article. Published on 06 spalio 2025. Downloaded on 2026-02-13 14:41:43.
This article is licensed under a Creative Commons Attribution-NonCommercial 3.0 Unported Licence.

including organic electrocatalysis, has remained unexplored. The synergistic influence of COF structure and properties on the EDL and interfacial charge/mass transfer kinetics in electrocatalysis remains insufficiently explored. We hypothesize that such fundamental understanding would be pivotal for developing the materials up to their promise as sustainable electrocatalysts, which would open up avenues for further engineering and eventual system integration.

Based on this premise, we report—for the first time—the use of COF-based electrodes to study the oxidation of benzylamine in aqueous medium as a model for green and sustainable organic electrosynthesis. In this proof-of-concept study, we established the structure–property role of COFs in EDL formation and manipulation for facilitating the catalysis. Two COFs featuring identical surface area, porosity and surface topography, but varying nitrogen content in their backbones, were assessed for their electrocatalytic activities. Hydrogen bonding and van der Waals' interactions between the N-rich COF, the electrolyte and the catalytic substrates resulted in selective adsorption of amines on the surface and pores of COF. This resulted in a notable change in the capacitive, impedance, and charge transfer properties of the electrode–electrolyte interface. These fundamental aspects have been thoroughly studied, and the reaction mechanism was duly established to ascertain the enhanced sustainability of the N-rich COF over the other material for catalysis. Finally, the catalytic protocol was further extended to other amine derivatives.

2 Results and discussion

Two COFs, TTA–BTPA-COF and TAPB–BTPA-COF, were synthesized *via* Schiff base condensation of 1,3,5-tris(2′-formylpyridyl-5′)benzene (BTPA–CHO) as the aldehyde linker with 4,4′,4″-(1,3,5-triazine-2,4,6-triyl)trianiline (TTA–NH_2) and 1,3,5-tris(4-aminophenyl)benzene (TAPB–NH_2), respectively (Fig. 1A and Scheme S3). The structures of COFs were analysed by powder X-ray diffraction (PXRD). The XRD patterns (Fig. 1B and C) reveal isomorphous crystalline structures of the two COFs. Both materials exhibit excellent crystallinity. A prominent peak at 4.05° corresponds to the (100) plane. Additionally, peaks located at 7.01°, 8.12°, 10.73°, 14.8° and 25.2° are attributed to the (110), (200), (210), (220), and (001) crystal planes, respectively. The experimental XRD results of two COFs exhibited an agreement with the density functional theory (DFT) optimised simulated AA-stacked model (for TTA–BTPA-COF, R_{wp} = 7.7% and R_p = 5.8%; for TAPB–BTPA-COF, R_{wp} = 5.1% and R_p = 3.5%), validating the layered AA-stacked structure of the materials.

Fourier transform infrared (FT-IR) spectroscopy further confirms the chemical structures of the COFs. The FT-IR peaks at 1700 cm^{-1} and 3400 cm^{-1} of the monomers, which can be attributed to carbonyl and N–H stretching vibrations of the aldehyde and amine functionalities, disappeared while a new peak at 1620 cm^{-1} appeared for TTA–BTPA-COF (Fig. S1). This indicates the formation of an imine bond through the

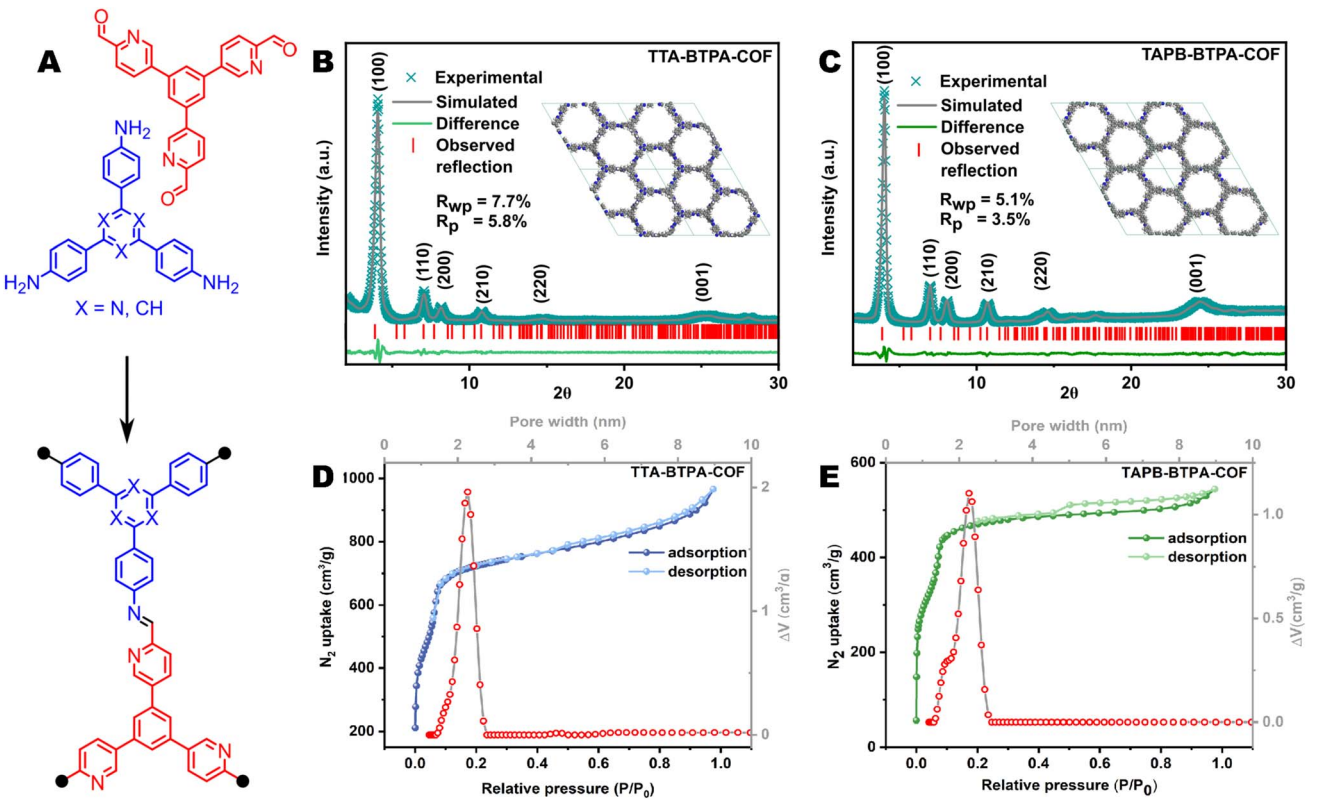

Fig. 1 (A) Synthetic scheme of TTA–BTPA-COF and TAPB–BTPA-COF. The PXRD patterns with corresponding simulated diffractogram and Pawley refinements of (B) TTA–BTPA-COF and (C) TAPB–BTPA-COF. N_2 sorption isotherms and pore size distribution of (D) TTA–BTPA-COF and (E) TAPB–BTPA-COF.

 This journal is © The Royal Society of Chemistry 2025

Open Access Article. Published on 06 spalio 2025. Downloaded on 2026-02-13 14:41:43.
This article is licensed under a Creative Commons Attribution-NonCommercial 3.0 Unported Licence.

condensation of the aldehyde and amine moieties.[26] A similar observation was recorded for TAPB–BTPA-COF as well (Fig. S2). Solid state ^{13}C cross-polarisation magic angle spinning (CP-MAS) NMR spectra (Fig. S3 and S4) further corroborate the existence of the imine bond (150 ppm) in both COFs. Additionally, the peaks located at 169 and 120–150 ppm in TTA–BTPA-COF are attributed to triazine and aromatic carbons, respectively, whereas similar peaks, except the one coming from triazine, can be deconvoluted from the ^{13}C CP-MAS NMR of TAPB–BTPA-COF.[27]

X-ray photoelectron spectroscopy (XPS) provided additional validation of the chemical structures of the COFs. The high-resolution C 1s XPS of TTA–BTPA-COF (Fig. S5) can be deconvoluted into two peaks at 285.3 and 283.9 eV, which are assigned to C=N species and graphitic C, respectively. On the other hand, N 1s XPS (Fig. S6) can be deconvoluted into two peaks as well, centred at 398 eV and 399.2 eV, which are assigned to the pyridinic/triazine C=N and imine, respectively.[28] This further proves the existence of the imine bond in COF. Similar XPS patterns were observed for TAPB–BTPA-COF as well (Fig. S7 and S8).

The porous properties were investigated by N_2 adsorption–desorption isotherm measurement at 77 K. Fig. 1D and E show a rapid increase in N_2 adsorption at low relative pressure for both COFs, referring to type I isotherm and the existence of micropores. The Brunauer–Emmett–Teller (BET) surface areas of TTA–BTPA-COF and TAPB–BTPA-COF are calculated to be 2048 $m^2 g^{-1}$ and 1359 $m^2 g^{-1}$. The distribution of pore size was determined by Quenched Solid Density Functional Theory (QSDFT) model, which showed an average pore diameter of 2.2 nm for both COFs. The analogous molecular structures of both COFs can justify a similar pore diameter. Additionally, the scanning and transmission electron microscopy (SEM and TEM) images indicated similar micro-tubular morphology of both COFs (Fig. S9 and S10). The TEM measurements show that for the TTA–BTPA-COF, small tubes are aggregated on the surface of large tubes, while for the TAPB–BTPA-COF, the surface remains smooth.

These combined analysis highlights that both TTA–BTPA- and TAPB–BTPA-COFs were successfully synthesized and had similar physicochemical properties, while TTA, containing a triazene unit, had an N-rich chemical backbone. We then tested how these properties can affect the sustainability of an electrochemical reaction when the COFs are used as electrodes in a systematic way. We probed the electrocatalytic oxidative C–N coupling of benzyl amine (BA) in 1 M aqueous KOH for this purpose. The COFs' catalytic performances were recorded in water (*i.e.*, 1 M aqueous KOH) first as a baseline, followed by the introduction of BA to the electrolyte to probe its oxidation. Linear sweep voltammetry (LSV) of two COFs showed that TAPB–BTPA-COF had a higher current density and early oxidation onset in 1 M KOH compared to TTA–BTPA (Fig. 2A). This suggests better water oxidation ability of TAPB–BTPA-COF.

After the addition of BA, the current density significantly increased for both COFs, with a reversal of their earlier catalytic performance. The LSV showed that in the presence of BA, TTA–BTPA-COF had a higher current density compared to TAPB–BTPA-COF. We recorded an 825% increase in current density for TTA–BTPA-COF at 2.5 V, whereas TAPB–BTPA-COF showed an increase of 38%. This suggests that TTA–BTPA-COF has higher selectivity towards BA in an aqueous medium over TAPB–BTPA-COF and performs more selective and sustainable oxidation of organic amines over water. This indicates a fundamental alteration in the electrode–electrolyte interface following the addition of BA to the aqueous medium, and the change is more prominent for the N-rich COF electrodes. To understand the structure–property relationships guiding the interfacial composition of the COF electrode–electrolyte systems, we used electrical double layer capacitance (EDLC) and Tafel analysis.

We consider that the abrupt change in polarization response upon BA addition is the result of the oxidation of BA, either as parallel to the water oxidation process or as the sole process by completely suppressing the water oxidation. Therefore, for the Tafel analysis, it was non-trivial to use 'overpotential' as a variable, and we plotted against the measured potential instead. This way, we can qualitatively explain the interfacial processes. As shown in Fig. 2B, the Tafel plots of the COFs in water and a water/BA mixture reveal crucial information on the interfacial processes. In the absence of BA, both COFs show similar exchange current density (j_0) and equilibrium potential, *viz.* 2.83 μA cm^{-2} and 0.175 V for TAPB–BTPA-COF, and 2.34 μA cm^{-2} and 0.196 V for TTA–BTPA-COF, respectively. After BA addition, TAPB–BTPA- and TTA–BTPA-COF showed decreased j_0 of 0.60 and 0.58 μA cm^{-2}, respectively. This *ca.* 80% decrease in j_0 following the addition of BA indicates the precedence of another dominant electrochemical process, where adsorption of foreign chemicals is involved.[29] As the addition of BA is the only change in the system, this indeed translates to the selective adsorption of BA from a water/BA mixture on both COF electrode surfaces. On the other hand, the equilibrium potential for TAPB–BTPA-COF can be recorded at 0.654 V in the water/BA system, whereas that of TTA–BTPA-COF was 0.398 V. These values suggested that TTA–BTPA-COF can come to equilibrium more easily than TAPB–BTPA-COF.

Parallel to these, the EDLC of the COFs measured in both systems (Fig. S11–S15) serves as another tool to complement the interfacial analyses obtained from the Tafel analyses. Fig. 2C reveals a 170% increase in EDLC of TTA–BTPA-COF from 96 to 260 μF cm^{-2} compared to 40% EDLC enhancement in TAPB–BTPA-COF from 150 to 210 μF cm^{-2}, following the introduction of BA into the electrolyte. As the COFs are serving as positively charged anodes, the increase in EDLC suggests a significant enhancement of the hydroxide anion concentration in their surface vicinity. Based on this and the Tafel analyses, we speculate that the introduction of BA is probably manipulating the solvation sphere of the hydroxide ions by replacing some water molecules from the inner hydration sphere of OH^- (Fig. 2G).[30] The water can assist this *via* additional van der Waals interactions from the secondary solvation shell. However, detailed theoretical studies are needed to confirm this claim. Regardless, the EDLC data inferred a greater interaction between BA and TTA–BTPA-COF than that between BA and TAPB–BTPA-COF, which can explain the augmented interfacial capacitance in the former system.

Open Access Article. Published on 06 spalio 2025. Downloaded on 2026-02-13 14:41:43.
This article is licensed under a Creative Commons Attribution-NonCommercial 3.0 Unported Licence.

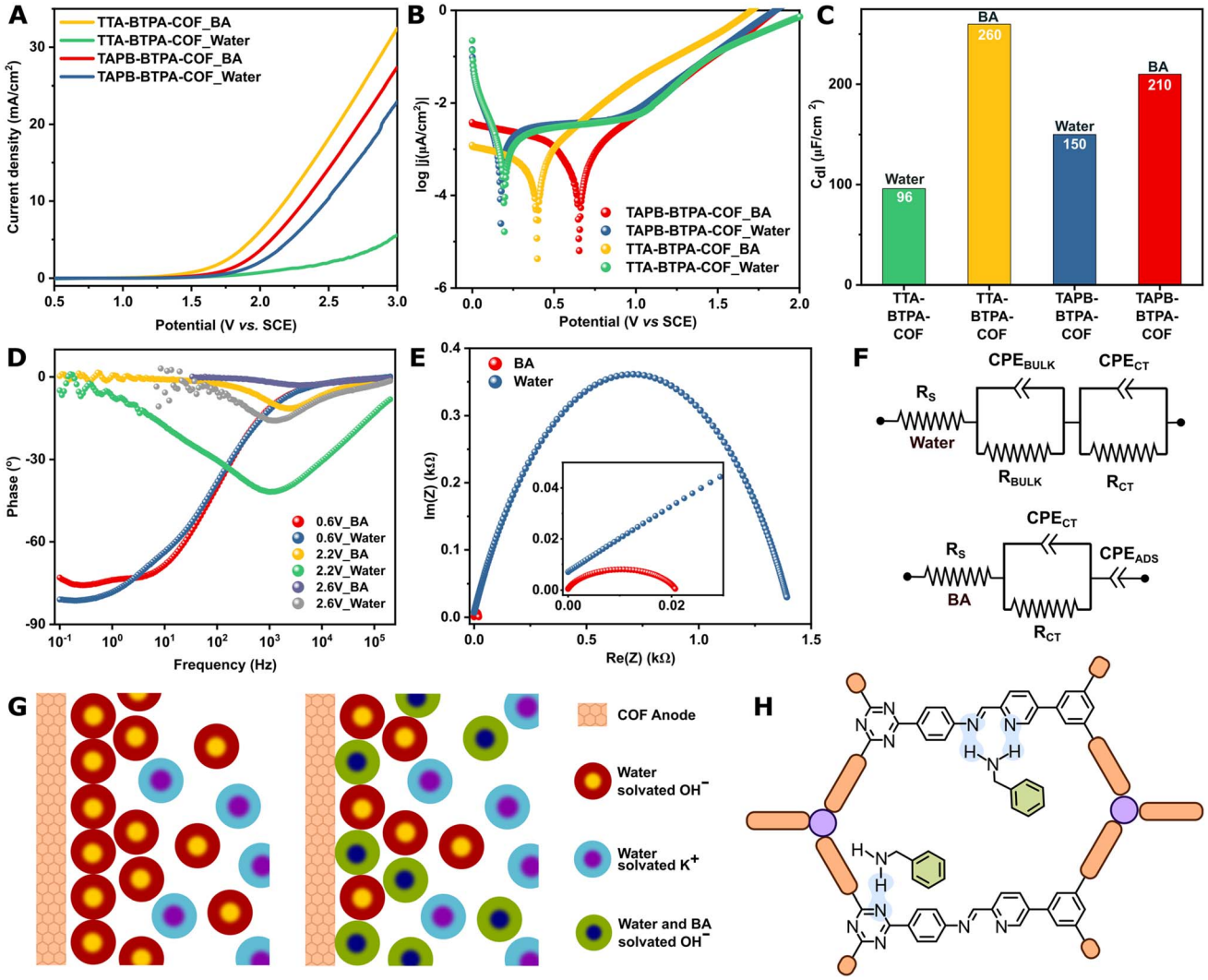

Fig. 2 (A) LSV curves; (B) Tafel-slope curves; (C) double-layer Capacitance (C_{dl}) values of TTA–BTPA-COF and TAPB–BTPA-COF with and without BA; (D) Bode plots for TTA–BTPA-COF with and without BA at different bias potentials; (E) Nyquist plots for TTA–BTPA-COF with and without BA at 2.2 V; (F) RC circuits of TTA–BTPA-COF with and without BA; (G) illustration of the interface between COF-anode surface and electrolyte with and without BA and (H) illustration for the hydrogen bond formation between TTA–BTPA-COF and BA.

At a given potential, the total current density (j_T) obtained during EDLC measurements is related to the cyclic voltammogram (CV) scan rate (ν) following eqn (1):

$$j_T = k\nu^{b(\psi)} \quad (1)$$

where the exponential factor 'b' is a function of potential (ψ). The value of b typically lies between 0.5 and 1, where $b = 0.5$ empirically represents purely faradaic contribution to the total current density and $b = 1$ indicates non-diffusion controlled capacitive component. Therefore, a plot of b-value *vs.* ψ at the non-faradaic zone gives an estimate of the potential dependency of adsorption or diffusion-controlled EDL behaviour. We adopted this technique to endorse the adsorption-controlled nature of the EDL for both COFs in the presence of BA. More faradaic contribution was recorded for both COFs in water, whereas their capacitive component significantly increased after the introduction of BA into the medium, reaching a b-value close to 1. This again signifies a greater adsorption-controlled EDL nature of the materials in the presence of BA. With increasing potential to 0.8 V, a gradual drop in the b-value was recorded in both COFs, indicating the precedence of faradaic current (Fig. S16 and S17). The b-value also indicated a better capacitive nature of TTA–BTPA-COF over TAPB–BTPA-COF, further suggesting the strong interaction between TTA–BTPA-COF and BA.

Impedance analysis provided additional corroboration of the interfacial dynamics.[31] The Bode plot (Fig. 2D) of TTA–BTPA-COF in the absence of BA measured at 0.6 V bias showed maximum phase shift at −0.4372 Hz. This peak, obtained at a non-faradic potential, is attributed to the maximum capacitive contribution from EDL at the electrode–aqueous OH^- interface. When BA is added to this system, two peaks are observed at −0.302 and 5.309 Hz at the same bias. This result suggests two

 This journal is © The Royal Society of Chemistry 2025

Open Access Article. Published on 06 spalio 2025. Downloaded on 2026-02-13 14:41:43.
This article is licensed under a Creative Commons Attribution-NonCommercial 3.0 Unported Licence.

types of interfacial contribution. The first one arises from the parent COF–aqueous OH^- interface, which has been shifted slightly towards lower frequency, possibly due to the change in local environment induced by BA. The new peak at higher frequency can be ascribed to the interaction between COF-amine solvated OH^-. Accordingly, the time constant values (Table S1) confirmed that the TTA–BTPA-COF can come to equilibrium much faster with the BA system than the pure aqueous interface.

Upon changing the bias to faradaic potentials 2.2 and 2.6 V, only one peak with a lower phase shift can be found, indicating gradual dissolution of the EDL as the oxidation proceeded. Of note, the time constant remained the same at ~130–140 μs for water oxidation at both faradaic potentials, whereas its value gradually decreased to 70 and 40 μs as the oxidation of BA proceeded, inferring faster kinetics of the BA oxidation at the TTA–BTPA-COF–water interface. Identical trends can be observed for TAPB–BTPA-COF as well. However, the time constants and phase shifts indicated relatively slower kinetics of BA-oxidation on TAPB–BTPA-COF (Fig. S18).

The Bode, EDLC, and Tafel data collectively suggest greater interaction between BA and TTA–BTPA-COF than that with TAPB–BTPA-COF. Given similar physical properties and traits of the COFs, we hypothesise that the selective adsorption and catalysis possibly result from the hydrogen bonding and van der Waals' attraction between the N-rich TTA–BTPA-COF and BA. To confirm this, FTIR of two COFs treated with BA were measured and compared with the FTIR of pure BA (Fig. S19–S22). The N–H stretching peak of the amine functionality showed a red shift of 76 cm^{-1} for TTA–BTPA-COF and 4 cm^{-1} for TAPB–BTPA-COF. This red shift can be explained by considering the existence of a hydrogen bonding interaction between BA and the COFs, which increases the bond order of the N–H bond in BA.[32] The shift is maximum for TTA–BTPA-COF, suggesting a stronger hydrogen bonding, possibly originating from the higher N-content of TTA–BTPA-COF (Fig. 2H).

Such interactions were expected to reduce the impedance of the materials by augmented charge transfer.[33] Accordingly, the Nyquist plots were obtained at 2.2 V, *i.e.*, at the beginning of the faradaic process (when total current density is 10 mA cm^{-2}, denoted as j_{10}). The corresponding equivalent Randles circuits used to fit the Nyquist plots are presented in Fig. 2F. The Nyquist plot (Fig. 2E and Table S2) indeed showed a significant reduction in the interfacial charge transfer resistance (R_{ct}) of TTA–BTPA-COF in the presence of BA. The 21.4 Ω R_{ct} was calculated in the presence of BA, which is *ca.* 45 times lower than that without BA (955.7 Ω). Additionally, the constant phase element (CPE), the frequency-dependent capacitive element contributing to the total impedance of TTA–BTPA-COF, was calculated to be 23.9 μF s^{a-1} in BA medium, while the value without BA is only 17.6 μF s^{a-1}. This increased capacitive trend accords well with the EDLC results. Moreover, an additional CPE of 2.04 F s^{a-1} can be recorded in the equivalent Randles circuit of TTA–BTPA-COF in the presence of BA. The appearance of such high capacitive elements can be attributed to the adsorption of BA on the COF surface (and pores) *via* strong hydrogen bonding. Therefore, strong adsorption of BA on COF's surface and lower charge transfer resistance collectively aided the oxidative performance of the system. The decline in impedance is also observed for TAPB–BTPA-COF (Fig. S23). However, this reduction in R_{ct} for TAPB–BTPA-COF is considerably smaller than that for TTA–BTPA-COF, indicating that the hydrogen-bonding interaction between TTA–BTPA-COF and BA is stronger than that between TAPB–BTPA-COF and BA, consistent with the FTIR results.

These mechanistic and interfacial insights clarified the role of COF's structure to precisely tune the electrode–medium interaction and interfacial composition, which is pivotal to catalyse a sustainable electrocatalytic process. With this knowledge, we conducted the electrocatalytic oxidative coupling of BA under a constant potential of 2.2 V (*vs.* SCE, when the current density is 10 mA cm^{-2}, j_{10}) at room temperature as an optimal sustainable condition (Fig. S24). After 6 hours of electrolysis, the BA underwent almost complete conversion, resulting in 99% yield of the desired *N*-benzylidenebenzylamine product. H_2 was produced at the cathode as the counter reaction, further increasing the sustainability and economic viability of the catalytic protocol. In contrast, the conversion by using TAPB–BTPA-COF as a catalyst was only 53%. As the reaction proceeded, the production of water-immiscible oily products made the reaction mixture turbid (Fig. S25). When the working electrode was replaced by blank FTO, a mere 30% BA conversion was observed, while water oxidation happened as the main reaction (Fig. S26).

Next, we extended the substrate scope of our protocol to other amines, where the reactions were conducted at constant potentials corresponding to the respective j_{10}, thereby maintaining the same concept of optimal sustainable catalytic conditions (Fig. S27–S30). The electron-rich 3- and 2-methoxybenzylamines showed a yield of 98% and 79%, respectively (**2** and **3**, Fig. 3). Benzyl amine demonstrated the highest yield (99%) (**1**) among all. The protocol remained true for aliphatic cyclohexanemethylamine as well (**4**). Furthermore, the secondary amine was also oxidised by TTA–BTPA-COF with an 88% yield (**5**).

We performed control experiments and reaction monitoring to understand the mechanism of the catalysis. Conducting the electrolysis in an H-cell confirmed that the product is obtained only in the anodic chamber, inferring the oxidative nature of the process (Fig. S31). Additionally, LC-MS analysis of the reaction mixture after a 3 h catalytic run showed the presence of two intermediates, *N*-benzylideneamine at 106*m*/*z* and 1-phenyl-*N*-(phenylmethyl)methanediamine at 212*m*/*z* (Fig. S32 and S33). In addition to these results, we have also confirmed significant adsorption of BA on the COF-electrode surface as evidenced by the impedance and Tafel analysis discussed earlier, which endorsed a fast COF → BA charge transfer process at 2.2 V. Based on these results, a plausible mechanism of the catalysis is proposed (Fig. 3). BA was initially absorbed on the surface of COF guided by hydrogen bonding and van der Waals' interaction, followed by its oxidation to generate *N*-benzylideneamine. This imine intermediate reacts with another BA molecule, yielding 1-phenyl-*N*-(phenylmethyl)methanediamine as a secondary intermediate. Oxidative dehydrogenation of this

Open Access Article. Published on 06 spalio 2025. Downloaded on 2026-02-13 14:41:43.
This article is licensed under a Creative Commons Attribution-NonCommercial 3.0 Unported Licence.

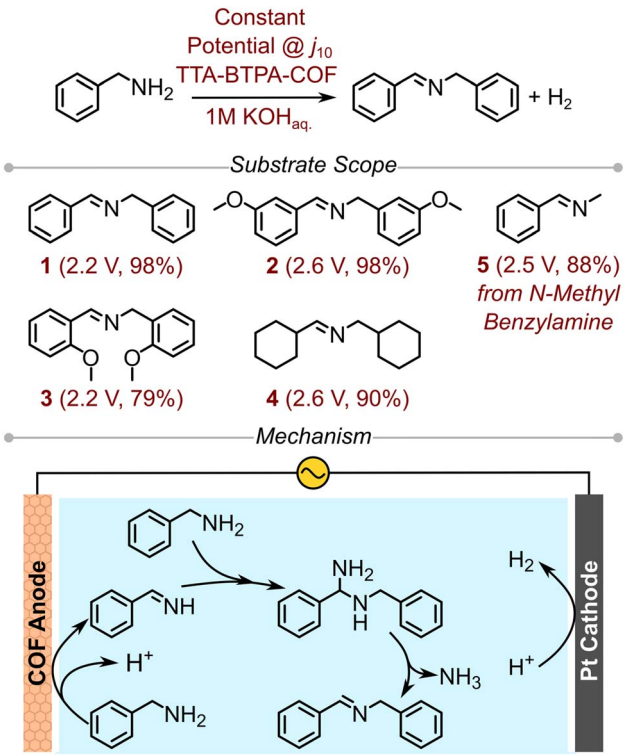

Fig. 3 Substrate scope of TTA–BTPA-COF catalysed selective oxidation of amines. Plausible mechanism for the electrocatalytic oxidative coupling of benzylamines into *N*-benzyl-1-phenyl-methanimines by TTA–BTPA-COF.

intermediate finally results in *N*-benzylidenebenzylamine. Parallel to this oxidative process, hydrogen evolution occurs at the cathode *via* the reduction of protons.

We further ascertained the key role of augmented BA adsorption on COF's surface and in pores. For this, we synthesized TTA–BTPA-COF-2, an alternate version of TTA–BTPA-COF featuring low porosity and surface area. The FTIR spectrum of TTA–BTPA-COF-2 (Fig. S34) is similar to that of TTA–BTPA-COF, indicating that both materials share the same chemical structure. Nonetheless, the XRD analysis (Fig. S35) revealed similar crystal patterns of both COFs; TTA–BTPA-COF-2 exhibited a high signal-to-noise ratio, suggesting less crystallinity and a higher amorphous fraction than TTA–BTPA-COF. This resulted in three times lower surface area and pore volume of TTA–BTPA-COF-2 (632.7 $m^2\ g^{-1}$ and 0.46 $cm^3\ g^{-1}$) as compared to that of TTA–BTPA-COF (Fig. S36). Accordingly, the EDLC of TTA–BTPA-COF-2 was calculated to be 87 mF cm^{-2} in the absence of BA and 201 mF cm^{-2} in the presence of BA (Fig. S37–S39), compared to 96 and 260 mF cm^{-2}, respectively, for TTA–BTPA-COF. This can be justified by considering that the larger surface area of TTA–BTPA-COF provides more area for the EDL to form, accommodating more charges and ions to accumulate near the electrode surface. Consequently, a higher number of charges can participate in the reaction, thus improving the reaction efficiency and kinetics. Additionally, the impedance analysis (Fig. S40) revealed that the R_{ct} of TTA–BTPA-COF-2 is almost five times higher than that of TTA–BTPA-COF, which implies that the ordered porosity and crystalline nature of TTA–BTPA-COF facilitate efficient electron transfer and benefit the reaction kinetics. Accordingly, the electrocatalytic BA oxidation TTA–BTPA-COF-2, conducted under the same conditions as TTA–BTPA-COF, showed only 51.4% conversion after 6 hours.

The stability of TTA–BTPA-COF during the catalytic run was studied. XRD of the reused COF showed identical diffraction patterns as the parent material (Fig. S41). Similarly, the FT-IR spectra of the parent and reused COF also showed an identical pattern (Fig. S42). Both these analyses showed that the structural integrity and chemical backbone of the COF retained during catalysis. The polarization response of the reused COF also matched well with the voltammogram of the as-synthesized material, indicating that the electrochemical behavior of TTA–BTPA-COF was sustained as well (Fig. S43).

3 Conclusion

In summary, this proof-of-concept study demonstrates the potential of COFs as sustainable electrocatalysts for electro-organic synthesis. We show how their physicochemical structure can be tuned to control the electrode–electrolyte interface, influencing both mass and charge transfer properties. Two COFs—TTA–BTPA-COF and TAPB–BTPA-COF—were synthesized as model systems to investigate the oxidative coupling of BA in water, alongside hydrogen production *via* a parallel reductive pathway. The nitrogen-rich TTA–BTPA-COF exhibited stronger hydrogen bonding with BA, leading to enhanced adsorption on the COF surface and within its pores. This resulted in selective, adsorption-controlled BA oxidation over water oxidation. The performance was marked by an 825% increase in current density at 2.5 V and a 170% enhancement in EDLC, significantly outperforming TAPB–BTPA-COF, which lacks such interactions. We thoroughly investigated the bias-dependent nature of these interactions and the associated dynamics of the electrical double layer. This allowed us to establish a clear structure–property relationship that governs the electrocatalytic behavior of COFs in a sustainable manner. Based on these mechanistic insights, we extended the catalytic protocol to other amine substrates. This first-of-its-kind study provides foundational understanding of how COFs can be designed and tuned for electrocatalytic applications. It highlights the advantages of their structural modularity in tailoring the electrochemical interface and controlling the kinetic and thermodynamic parameters that drive electrocatalysis.

Author contributions

Rundong Wang: conceptualization; investigation; formal analysis, data curation; visualization; validation; writing original draft, review & editing. Ipsita Nath: formal analysis; investigation; writing original draft, review & editing; supervision. Jeet Chakraborty: investigation, review & editing. Linyang Wang: formal analysis. Pascal Van Der Voort: supervision; funding acquisition; review & editing.

This journal is © The Royal Society of Chemistry 2025

Open Access Article. Published on 06 spalio 2025. Downloaded on 2026-02-13 14:41:43.
This article is licensed under a Creative Commons Attribution-NonCommercial 3.0 Unported Licence.

Conflicts of interest

There are no conflicts of interest to declare.

Data availability

The data supporting this article has been included as part of the Supplementary information (SI). Supplementary information: additional experimental details, characterization data, and supporting figures that complement the results presented in the main text. See DOI: **https://doi.org/10.1039/d5ta05552k**.

Acknowledgements

PVDV, IN, JC, RW and LW acknowledge the FWO-Vlaanderen for research grant G020521N. PVDV and IN acknowledge the research board of UGent (BOF) through a Concerted Research Action (GOA010-17). RW and LW acknowledge the support from the China Scholarship Council (CSC202106880011, CSC202108110055). JC acknowledges UGent for the BOF post-doctoral grant (2022.0032.01). PVDV acknowledges UGent BASBOF BOF20/BAS/015 for the powder X-ray diffractometer.

References

1 Z. Lin, U. Dhawa, X. Hou, M. Surke, B. Yuan, S.-W. Li, Y.-C. Liou, M. J. Johansson, L.-C. Xu, C.-H. Chao, X. Hong and L. Ackermann, *Nat. Commun.*, 2023, **14**, 4224.
2 B. A. Frontana-Uribe, R. D. Little, J. G. Ibanez, A. Palma and R. Vasquez-Medrano, *Green Chem.*, 2010, **12**, 2099–2119.
3 J. Utley, *Chem. Soc. Rev.*, 1997, **26**, 157–167.
4 W. Zeng, Y. Wang, C. Peng and Y. Qiu, *Chem. Soc. Rev.*, 2025, **54**, 4468–4501.
5 C. Ma, P. Fang, Z.-R. Liu, S.-S. Xu, K. Xu, X. Cheng, A. Lei, H.-C. Xu, C. Zeng and T.-S. Mei, *Sci. Bull.*, 2021, **66**, 2412–2429.
6 L. F. T. Novaes, J. Liu, Y. Shen, L. Lu, J. M. Meinhardt and S. Lin, *Chem. Soc. Rev.*, 2021, **50**, 7941–8002.
7 D. Pollok and S. R. Waldvogel, *Chem. Sci.*, 2020, **11**, 12386–12400.
8 S. Fleischmann, J. B. Mitchell, R. Wang, C. Zhan, D.-e. Jiang, V. Presser and V. Augustyn, *Chem. Rev.*, 2020, **120**, 6738–6782.
9 V. Vivier and M. E. Orazem, *Chem. Rev.*, 2022, **122**, 11131–11168.
10 S. Wang, J. Zhang, O. Gharbi, V. Vivier, M. Gao and M. E. Orazem, *Nat. Rev. Methods Primers*, 2021, **1**, 41.
11 A. C. Rowett, S. G. Sweeting, D. M. Heard and A. J. J. Lennox, *Angew Chem. Int. Ed. Engl.*, 2024, **63**, e202400570.
12 V. Flexer and L. Jourdin, *Acc. Chem. Res.*, 2020, **53**, 311–321.
13 S. Ghosh, A. Nakada, M. A. Springer, T. Kawaguchi, K. Suzuki, H. Kaji, I. Baburin, A. Kuc, T. Heine, H. Suzuki, R. Abe and S. Seki, *J. Am. Chem. Soc.*, 2020, **142**, 9752–9762.
14 K. T. Tan, S. Ghosh, Z. Wang, F. Wen, D. Rodríguez-San-Miguel, J. Feng, N. Huang, W. Wang, F. Zamora, X. Feng, A. Thomas and D. Jiang, *Nat. Rev. Methods Primers*, 2023, **3**, 1.
15 P. J. Waller, F. Gándara and O. M. Yaghi, *Acc. Chem. Res.*, 2015, **48**, 3053–3063.
16 S. Ghosh, H. Küçükkeçeci, R. P. Paitandi, V. Weigelt, V. Dippold, S. Seki and A. Thomas, *J. Mater. Chem. A*, 2024, **12**, 247–255.
17 X. Cui, S. Lei, A. C. Wang, L. Gao, Q. Zhang, Y. Yang and Z. Lin, *Nano Energy*, 2020, **70**, 104525.
18 C.-Y. Lin, D. Zhang, Z. Zhao and Z. Xia, *Adv. Mater.*, 2018, **30**, 1703646.
19 T. Sun, J. Xie, W. Guo, D.-S. Li and Q. Zhang, *Adv. Energy Mater.*, 2020, **10**, 1904199.
20 B. Rehl, E. Ma, S. Parshotam, E. L. DeWalt-Kerian, T. Liu, F. M. Geiger and J. M. Gibbs, *J. Am. Chem. Soc.*, 2022, **144**, 16338–16349.
21 L. Fumagalli, A. Esfandiar, R. Fabregas, S. Hu, P. Ares, A. Janardanan, Q. Yang, B. Radha, T. Taniguchi, K. Watanabe, G. Gomila, K. S. Novoselov and A. K. Geim, *Science*, 2018, **360**, 1339–1342.
22 B. Han, X. Ding, B. Yu, H. Wu, W. Zhou, W. Liu, C. Wei, B. Chen, D. Qi, H. Wang, K. Wang, Y. Chen, B. Chen and J. Jiang, *J. Am. Chem. Soc.*, 2021, **143**, 7104–7113.
23 Y. Ma, Y. Fu, W. Jiang, Y. Wu, C. Liu, G. Che and Q. Fang, *J. Mater. Chem. A*, 2022, **10**, 10092–10097.
24 P. García-Arroyo, E. Martínez-Periñán, J. J. Cabrera-Trujillo, E. Salagre, E. G. Michel, J. I. Martínez, E. Lorenzo and J. L. Segura, *Nano Res.*, 2022, **15**, 3907–3912.
25 D. Li, C. Li, L. Zhang, H. Li, L. Zhu, D. Yang, Q. Fang, S. Qiu and X. Yao, *J. Am. Chem. Soc.*, 2020, **142**, 8104–8108.
26 Q. Sun, S. Jiang, H. Niu, Y. Li, X. Wu, Y. Shi and Y. Cai, *J. Mater. Chem. A*, 2024, **12**, 5254–5260.
27 F. Huang, Y. Wang, X. Dong and X. Lang, *J. Mater. Chem. A*, 2024, **12**, 7036–7046.
28 J. Hou, H. Liu, M. Gao, Q. Pan and Y. Zhao, *Angew. Chem., Int. Ed.*, 2025, **64**, e202414566.
29 M. Yan, N. Dong, X. Zhao, Y. Sun and H. Pan, *ACS Energy Lett.*, 2021, **6**, 3236–3243.
30 B. Chen, I. Ivanov, J. M. Park, M. Parrinello and M. L. Klein, *J. Phys. Chem. B*, 2002, **106**, 12006–12016.
31 Y. Jin, E. Zhou, T. Ueki, D. Zhang, Y. Fan, D. Xu, F. Wang and D. R. Lovley, *Angew Chem. Int. Ed. Engl.*, 2023, **62**, e202309005.
32 M. Rozenberg, G. Shoham, I. Reva and R. Fausto, *Phys. Chem. Chem. Phys.*, 2005, **7**, 2376–2383.
33 Z. Li, T. Tsuneyuki, R. P. Paitandi, T. Nakazato, M. Odawara, Y. Tsutsui, T. Tanaka, Y. Miyake, H. Shinokubo, M. Takagi, T. Shimazaki, M. Tachikawa, K. Suzuki, H. Kaji, S. Ghosh and S. Seki, *J. Am. Chem. Soc.*, 2024, **146**, 23497–23507.